THE JOURNAL OF PHYSICAL CHEMISTRY C

pubs.acs.org/JPCC Article

How Flexibility of the Nanoscale Solvophobic Confining Material Promotes Capillary Evaporation of Ionic Liquids

Harender S. Dhattarwal, Richard C. Remsing, and Hemant K. Kashyap*

Cite This: J. Phys. Chem. C 2020, 124, 4899–4906 Read Online

ACCESS | Metrics & More | Article Recommendations

ABSTRACT: Capillary evaporation of ionic liquids in nanoscale confinement is an important process relevant to self-assembly and energy storage applications. Most studies focus on understanding ionic liquids confined by rigid materials, but the flexibility of the materials can also impact the thermodynamics of confinement. In this work, we investigate the effects of flexibility of confining surfaces on the structure and free energy underlying capillary evaporation of the ionic liquid 1-ethyl-3-methylimidazolium tetrafluoroborate ([EMIM][BF_4]) in nanoscale solvophobic confinements. We employ indirect umbrella sampling to estimate the free energy profiles for [EMIM][BF_4] between both rigid and flexible square confining surfaces at several intersheet separations. The analysis of these free energy profiles shows that capillary evaporation of [EMIM][BF_4] is enhanced by the introduction of flexibility to the confining sheets. We examine the number density profiles for the ionic species in the confinement, which show distinct structural layering for different separations. By additionally characterizing the orientational ordering of cations in confinement, we quantify significant structural changes that occur as the intersheet distance is reduced and as capillary evaporation occurs at fixed confinement. We find that flexibility of the confining material also impacts the structural changes that occur as the ionic liquid evaporates from the intersheet region.

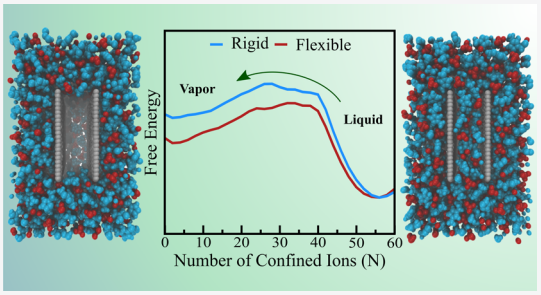

1. INTRODUCTION

Ionic liquids (ILs) have a wide electrochemical window and high chemical and thermal stability, which make them perfect for energy storage in batteries, photoelectrochemical cells, and heat storage devices.[1−10] Another important characteristic of ILs to control the mechanism of aggregation of small and large nonpolar solutes has gained attention recently.[11,12] The solvophobic interactions of ILs with nanoscale solutes, such as graphene, result in dispersion at lower concentrations and aggregation at higher concentrations.[13−15] It has been found that the interaction of solvents confined between sufficiently sized solvophobic nanoscale materials results in strong attractive forces between the materials,[16] which drives the dewetting of the electrolyte from nanoporous electrodes,[17] capillary evaporation of the solvent from nanoscale conduits, protein−ligand binding, block copolymer assemblies in aqueous and nonaqueous liquids, and many other physical phenomena.[14,18−22]

Many distance-dependent studies of capillary evaporation have discussed that when nanoscale solvophobic confining surfaces come into close proximity, the vapor state of the solvent confined between them becomes more stable.[23−26] Huang et al. showed that the critical distance at which liquid and vapor phases of water are equally stable is dependent on the size of the confining surfaces.[27] Altabet et al. showed through forward flux sampling that the free energy barrier for transitions between these states in water is affected by introducing flexibility to the confining walls.[28] They also revealed the effect of flexibility of confining surfaces on the kinetics and thermodynamics of capillary evaporation of water and found that the rate of evaporation is increased by multiple folds with increased flexibility. However, analogous theoretical studies exploring the effects of surface flexibility on capillary evaporation in nonaqueous solvents are scarce in the literature. Because of the ubiquity of confinement in materials applications, it is important to explore these effects in nonaqueous solvents, such as ILs. The behavior of ILs in confinement has been widely studied in the literature, and the understanding gained has helped to employ these solvents in various applications, especially in electric double-layer capacitors (EDLCs) and self-assembly.[13−15,29−33] Moreover, nanoscale confinement conducive to capillary evaporation is prevalent in these applications, and the study of these processes in ILs is critical to their deployment in functional materials. In this spirit, we have performed detailed enhanced molecular dynamics simulations to examine the effects of flexibility of the confining material on the behavior of IL 1-ethyl-3-methylimidazolium tetrafluoroborate ([EMIM][BF_4]).

Received: December 20, 2019
Revised: January 26, 2020
Published: February 5, 2020

This particular solvent represents the class of alkylimidazolium-based ILs, which are well known for their applications in self-assembly and electrochemical devices such as EDLCs.[34−40] The ease of availability and well-documented bulk and interfacial structure make this IL well-suited for our initial studies presented here.[41−44]

2. SIMULATION DETAILS

The initial simulation cell was a 6.5 nm × 10 nm × 6.5 nm tetragonal box, consisting of 1570 ion pairs of $[EMIM][BF_4]$, generated using PACKMOL.[45] The chemical structures of $[EMIM]^+$ and $[BF_4]^-$ ions used in the present study are shown in Figure 1. The average end-to-end size along the longest axis

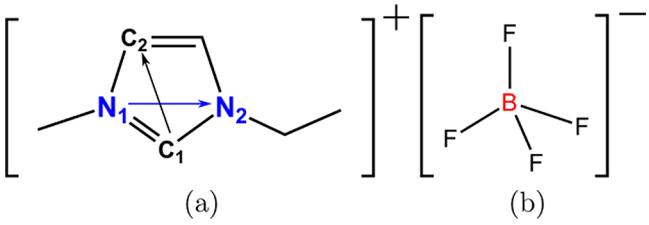

Figure 1. Structure of (a) $[EMIM]^+$ and (b) $[BF_4]^-$ used in the present study.

of $[EMIM]^+$ is ∼0.75 nm, and for $[BF_4]^-$, it is ∼0.19 nm. All-atom molecular dynamics simulations were carried out using GROMACS 5.1.4 package.[46,47] The bulk IL system was equilibrated for 16 ns in isobaric−isothermal (*NPT*) ensemble at 310 K temperature and 1 bar pressure. In order to maintain the pressure and temperature of the system, Berendsen barostat and Berendsen thermostat[48] were used for the initial 8 ns and Parrinello−Rahman barostat[49] and Nosé−Hoover[50,51] thermostat were used for the rest of the equilibration, respectively.

A pair of sheets (3 nm × 3 nm), each consisting of 572 hexagonally packed (lattice constant 0.14 nm) carbon atoms and separated by a distance d nm in the z-direction, were generated using an in-house program and placed in the bulk IL along the xy-plane using VMD software.[52] Nearest neighbors of the sheet were bonded with a harmonic spring with constant K, such that the flexibility of the confinement can be tuned by changing this constant. Herein, moderately stiff carbon sheets were taken with a K value set to be 30,000 kcal mol^{-1} nm^{-2}, comparable to the intermediate stiffness plates studied by Altabet et al.[28] For flexible carbon confinement, the atoms on the edges of sheets were fixed in the xy-plane such that the separation between the corresponding edges of opposite sheets was constant.

The value of Lennard-Jones (LJ) interaction parameter, σ, for the sheet atoms was adapted from ref 53. It has been shown that the short- and long-range interactions of carbon sheets with ILs are well-captured by the LJ parameters.[13] Therefore, in order to ensure a significantly solvophobic surface model, the value of the LJ interaction potential was chosen (ϵ = 0.022 kJ mol^{-1}) to be considerably lower than the value for graphene sheets (0.23 kJ mol^{-1}).[13] A liquid−vapor interface was created along the y-direction to mimic a constant pressure ensemble by providing a vacuum of 2.5 nm on each side of the IL box. The liquid−vapor interface acts as a natural barostat with a constant pressure equal to that at liquid−vapor coexistence. In order to avoid drift in the direction perpendicular to the liquid−vapor interface, a neutral repulsive carbon wall consisting of 2116 atoms arranged on a square lattice was placed above the interface, as reported in previous work.[26,53]

The force field parameters for $[EMIM]^+$ and $[BF_4]^-$ were taken from OPLS-AA/AMBER force fields proposed by Lopes and Paduá (CL&P).[54] The Lorentz−Berthelot combination rules were used to compute cross-interaction terms of LJ potentials. A standard 3D periodic boundary condition and minimum image convention were applied. The biased simulations were run for 50 ns, and equations of motion were integrated using the leap-frog algorithm with a time step of 1 fs. The last 40 ns of the trajectory saved at every 1 ps was used for the analysis. The cutoff radius for the evaluation of short-ranged interactions was set to 1.2 nm. Coulomb interactions were evaluated using the particle mesh Ewald summation technique with an interpolation order of 6 and a Fourier grid spacing of 0.08 nm. The Nosé−Hoover thermostat with a relaxation constant of 0.2 ps was used to maintain a constant temperature of 310 K throughout the simulations.

Non-Boltzmann sampling was used to probe the density fluctuations between the confining sheets. The free energy landscape underlying capillary evaporation of the IL was estimated by computing the probability $P_v(N)$ of finding N

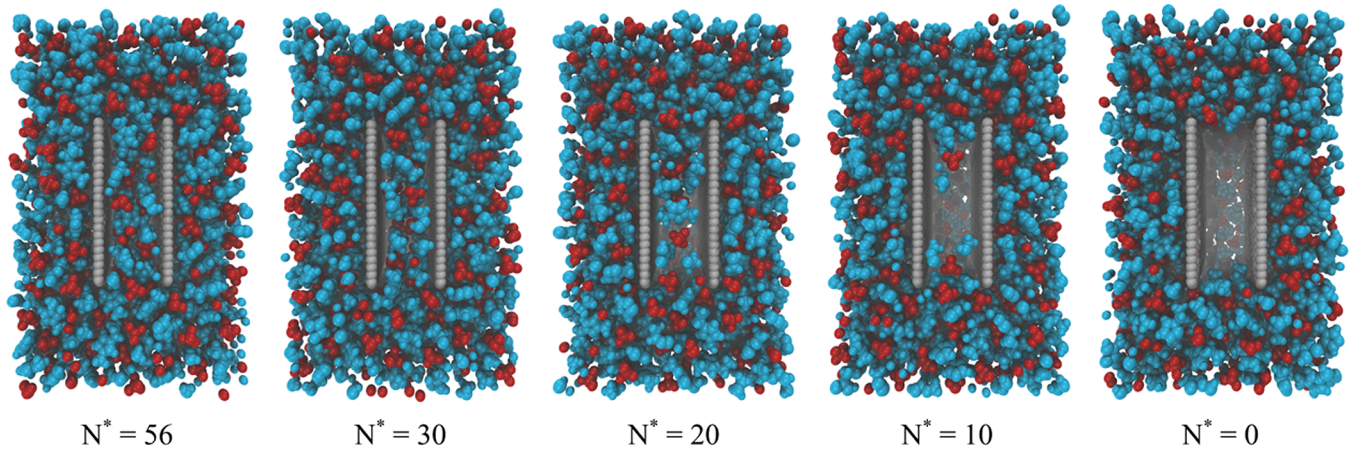

Figure 2. Representative simulation snapshots for $[EMIM][BF_4]$ IL between nanoscale solvophobic sheets separated at 1.3 nm. Blue and red beads represent cations and anions, respectively; silver beads represent carbon sheets.

https://dx.doi.org/10.1021/acs.jpcc.9b11755
J. Phys. Chem. C 2020, 124, 4899−4906

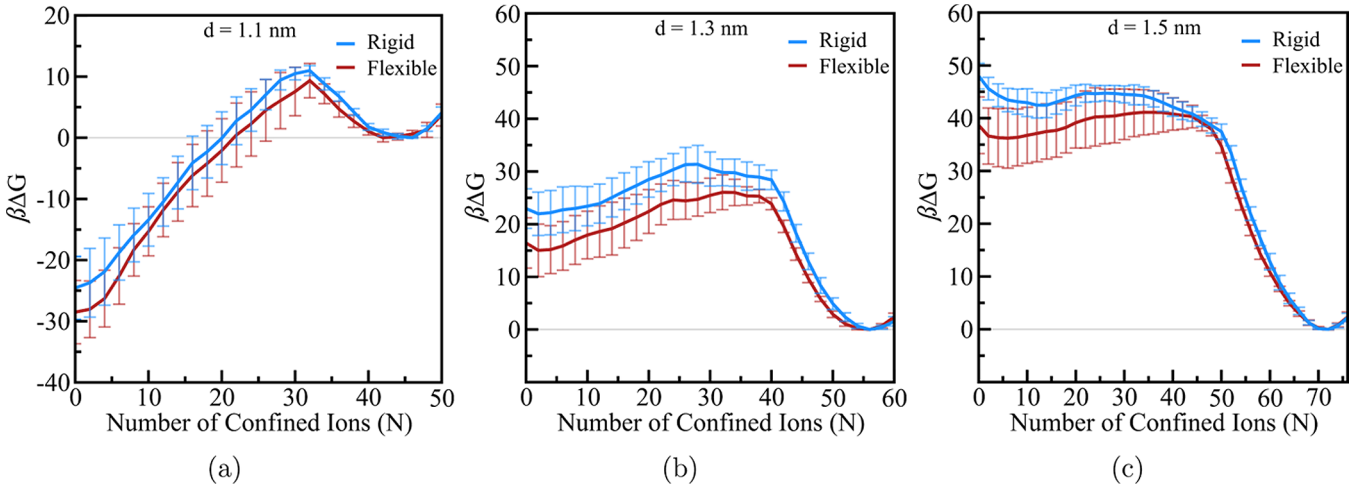

Figure 3. Simulated free energy profiles as a function of number of ions in the confinement.

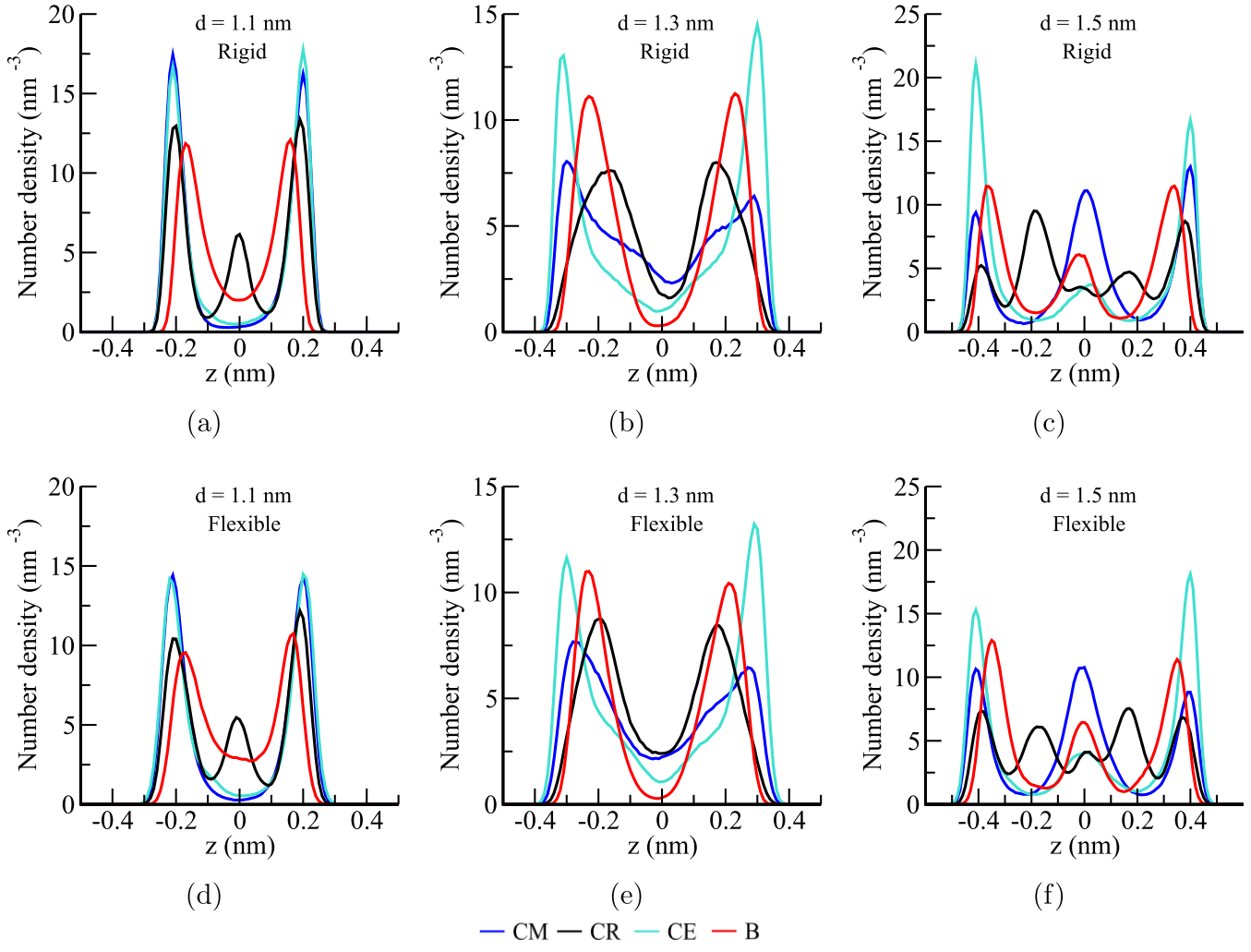

Figure 4. Number density distribution of atomic sites of [EMIM][BF_4] computed for configurations with N corresponding to the liquid basin between solvophobic rigid and flexible nanoscale confinements.

ions in the volume v between the two sheets for varying intersheet distances, d. However, the order parameter N is discrete and cannot be readily used to bias molecular dynamics simulations with N-dependent forces. Instead, the discrete order parameter N was sampled using the indirect umbrella sampling (INDUS) approach, where a biasing potential is applied on $\tilde{N}$, which is a coarse-grained, continuous variant of the order parameter N.[55,56] INDUS uses a harmonic biasing potential, $U(\tilde{N}) = \kappa(\tilde{N} - \tilde{N}^*)^2/2$. Here, we vary $\tilde{N}$ over a range of −2 to 76 with an interval of 2. The INDUS potential

https://dx.doi.org/10.1021/acs.jpcc.9b11755
J. Phys. Chem. C 2020, 124, 4899−4906

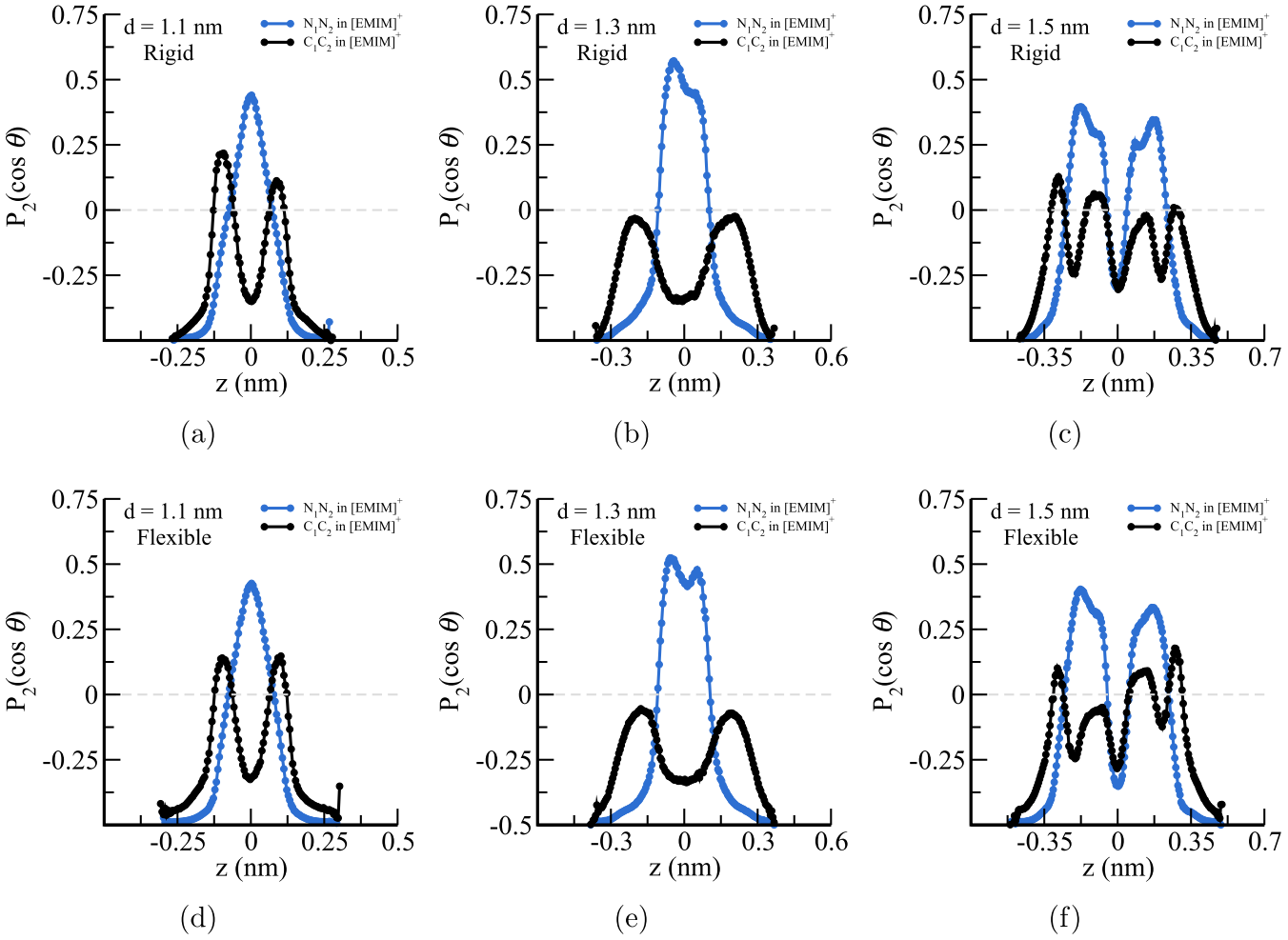

Figure 5. Distance-dependent orientational order parameter defined for $\overrightarrow{N_1N_2}$ and $\overrightarrow{C_1C_2}$ vectors in the $[EMIM]^+$ cation ring between solvophobic rigid and flexible nanoscale confinements for configurations with N corresponding to the liquid basin.

was applied only on the boron atom of $[BF_4]^-$ and the ring nitrogen atom of $[EMIM]^+$ which is closest to the center of mass of the cation. Simulation snapshots representing the transition from the liquid to vapor phase of $[EMIM][BF_4]$ between nanoscale solvophobic sheets separated at 1.3 nm are shown in Figure 2. The free energies $\Delta G(N) = -\beta^{-1} \ln P_v(N)$ were estimated from the INDUS simulations using the weighted histogram analysis method, where $\beta = 1/k_BT$ and k_B is the Boltzmann constant.[57] One million frames were used to compute each free energy profile. Error bars were estimated through block averaging, where 8 blocks were chosen with an interval of 5 ns. The orientational order of the $[EMIM]^+$ ions within the rigid and flexible confinements was quantified by computing the orientational order parameter defined as

$$P_2(\cos\theta) = \langle 1.5 \cos^2\theta - 0.5 \rangle \quad (1)$$

where θ is the angle between the vector normal to the plane of the confining sheets and a vector defined in the cation ring (see Figure 1).

3. RESULTS AND DISCUSSION

3.1. Free Energy Profiles. The free energy, $\Delta G(N;d)$, as a function of the number of ions between the nanoscale solvophobic confining surfaces, N, is plotted for three different sheet separations, d, and for rigid and flexible plates in Figure 3. Here, minima at high and low N values define the liquid and vapor phases of $[EMIM][BF_4]$ in the confinement, respectively, which are separated by a significant free energy barrier. Note that all the profiles are shifted to set the free energy of the liquid basin equal to zero. Our results are in good agreement with the previous work that used the total number of IL heavy atoms to define N and $\tilde{N}$.[26]

The free energy profiles, $\Delta G(N;d)$, are shown in Figure 3a–c for d = 1.1 nm, d = 1.3 nm, and d = 1.5 nm, respectively. All free energy profiles exhibit basins corresponding to liquid (high N) and vapor (low N) basins, with a substantial free energy barrier separating these two states. At larger separations, the liquid phase of $[EMIM][BF_4]$ is stable in the confinement and the vapor is metastable. The relative free energy of the vapor phase decreases with decreasing d. The sheet separation at which both the liquid and vapor phases have the same free energy is termed as critical distance, d_c. Because the liquid is stable for d = 1.3 nm and the vapor is stable for d = 1.1 nm, the values of d_c for both the rigid and flexible sheets are located between 1.1 and 1.3 nm, though not necessarily at the midpoint. Moreover, d_c will be smaller for the rigid sheets, as discussed in previous work.[58] Below d_c, the liquid phase becomes metastable with respect to the vapor (Figure 3a). The free energy barrier separating the liquid and vapor phases lowers with decreasing d.[26,53] At significantly

https://dx.doi.org/10.1021/acs.jpcc.9b11755
J. Phys. Chem. C 2020, 124, 4899−4906

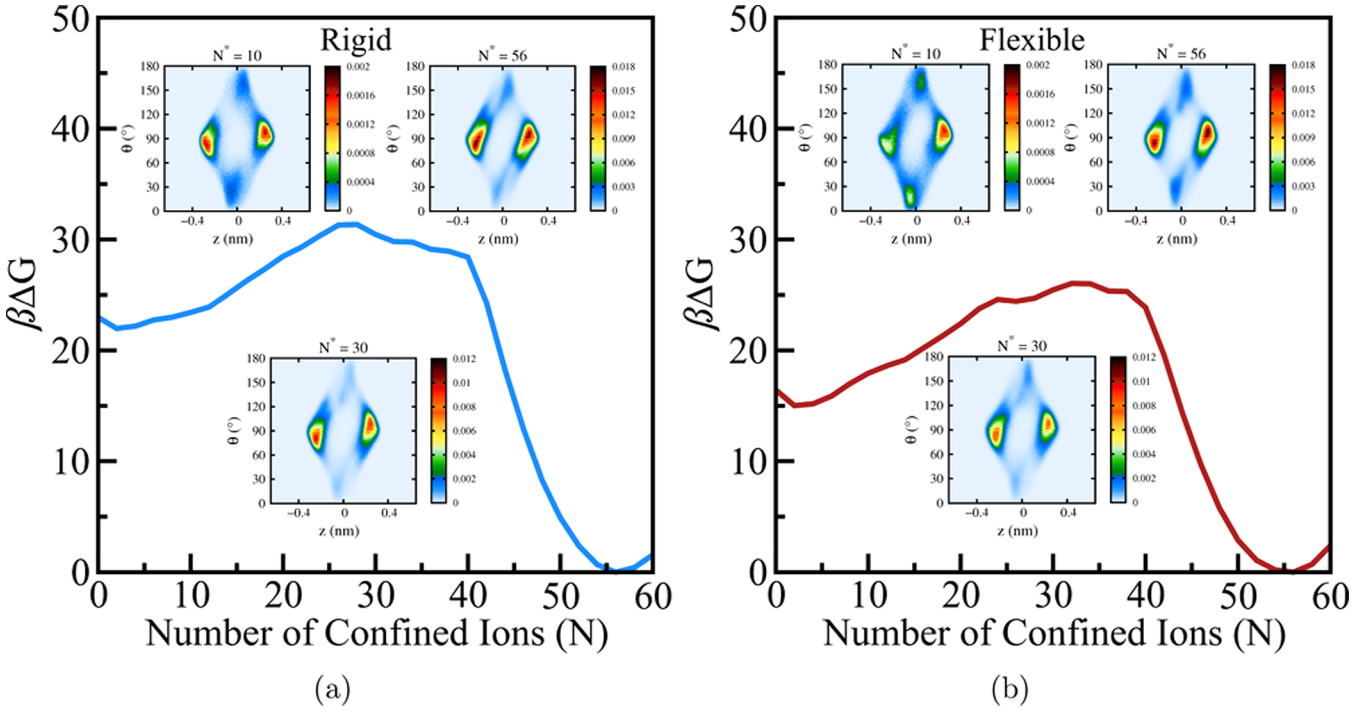

Figure 6. Contour plot of number density profile for the $\overrightarrow{N_1N_2}$ vector in the $[EMIM]^+$ cation ring between solvophobic nanoscale confinements for $[EMIM][BF_4]$ densities changing from the liquid to vapor phase plotted for (a) rigid and (b) flexible confinements. For all cases shown here, N^* and $\langle N \rangle$ differ by less than 1.

smaller d, the barrier disappears and spontaneous capillary evaporation occurs.

The introduction of flexibility to the confining sheets stabilizes the vapor state for all d-values studied here and has little effect on the liquid basin beyond a slight increase in its width. This is consistent with the theoretical predictions of Altabet and Debenedetti; for low N, there will exist a pressure difference between the bulk and the confined, low-density or vapor-like phase, and this pressure difference combined with surface tension forces will deform the flexible plates, effectively decreasing the confining volume as N is lowered.[58] This decrease in the volume as N is lowered results in a stabilization of the vapor phase with respect to what is expected for rigid plates, that is, the effective d is lower for flexible plates than for rigid plates at low N, while they are equal at liquid-like N-values.

3.2. Number Density Profiles and Orientational Order Parameter. Number density profiles of the boron (B) atom of the anion, terminal carbon of the ethyl group (CE), central carbon of the ring (CR), and the terminal carbon of the methyl group (CM) of the cation for rigid and flexible solvophobic confinements at different separations are depicted in Figure 4a–f. The number density distributions are evaluated for systems with N corresponding to the liquid basin.

The number density profiles for atoms between rigid and flexible sheets separated by 1.1 nm are shown in Figure 4a,d, respectively. The peak positions of CM, CR, and CE densities overlap nearest to the confining surfaces (at $z = \pm 2$ nm), which suggests that cation rings are oriented parallel to the sheets. Also, the comparatively less pronounced peak for CR near the middle of the confined space ($z = 0$ nm), along with small densities of CM and CE, additionally suggests that some cations also adapt a perpendicular orientation, such that the ethyl and methyl groups interact with different sheets, and the ring remains at the middle of the confined region. We also observe two peaks for the anion close to the confining surfaces, indicating a bilayer distribution of anions between the confining sheets at this interplate spacing. These observations suggest highly structured arrangements of ions in solvophobic confinement at $d = 1.1$ nm.

As the sheet separation is increased to $d = 1.3$ nm (Figure 4b,e), we observe broader peaks for cationic species. This suggests a weakening in the structural ordering of $[EMIM]^+$ between sheets. However, the two sets of peaks in the density profiles for all the species indicate an approximately bilayer distribution of $[EMIM]^+$ and $[BF_4]^-$ between carbon sheets separated at $d = 1.3$ nm.

At the largest sheet separation studied here, $d = 1.5$ nm (Figures 4c and 5f), the ring carbon atom, CR, shows five peaks within the confined space. However, the alkyl carbons and the anion B atoms exhibit three layers in their respective density distributions. The coinciding peak positions of the CR, CE, and CM densities near the sheets suggest that the cation rings at this location are oriented parallel to the confining plates. A similar parallel orientation is also observed in the middle of the interplate region, near $z = 0$ nm. The presence of the second and fourth CR peaks indicates that cations at the sheet surface also adopt perpendicular orientations, such that the alkyl ends are either at the interface or the center of the confinement. Our results are consistent with the structural layering observed for $[EMIM][BF_4]$ and other ILs when confined between carbon sheets.[26,59] Moreover, recent study on water between hydrophobic confinements shows that the structural changes influence the kinetics of capillary evaporation of water from the confinements.[60]

To further understand the structural ordering of $[EMIM]^+$ between the solvophobic sheets, we examine the z-dependence of two orientational order parameters, the angle θ formed by

https://dx.doi.org/10.1021/acs.jpcc.9b11755
J. Phys. Chem. C 2020, 124, 4899−4906

the normal to the sheet surface and either the $\overrightarrow{N_1N_2}$ or $\overrightarrow{C_1C_2}$ vector in the cation rings, as shown in Figure 5a–f. For d = 1.1 nm (Figure 5a,d), we observe two major orientations of $[EMIM]^+$. The negative values of $P_2(\cos\theta)$ near the surface for both $\overrightarrow{N_1N_2}$ and $\overrightarrow{C_1C_2}$ correspond to parallel orientations of $[EMIM]^+$ rings to the sheet. Moreover, $P_2(\cos\theta)$ is positive for $\overrightarrow{N_1N_2}$ while that for $\overrightarrow{C_1C_2}$ is negative for $z \approx 0$ nm. This corresponds to slightly perpendicular average orientation of the $[EMIM]^+$ cations at the center of the confined region.

Similar but broadened profiles of $P_2(\cos\theta)$ are found for d = 1.3 nm, as shown in Figure 5b,e. We again observe parallel orientations of $[EMIM]^+$ rings near the sheets and perpendicular orientations near the center for both rigid and flexible confinements. However, the peaks in $P_2(\cos\theta)$ corresponding to the central perpendicular orientation of the cation rings are broader and have higher values than the respective peaks in $P_2(\cos\theta)$ for d = 1.1 nm. These observations suggest that the perpendicular orientation of cation rings at the middle of the confinement is relatively more favorable when the sheets are separated by 1.3 nm.

The behavior of $P_2(\cos\theta)$ for d = 1.5 nm is more complex because of the appearance of several orientationally ordered layers, as shown in Figure 5c,f for rigid and flexible sheets, respectively. Here, we observe two troughs in the orientational order parameter for $\overrightarrow{N_1N_2}$ vectors in $[EMIM]^+$ nearest to the sheets and one at the center of the confined space. The troughs closest to the confining walls have values around −0.5, corresponding to parallel orientations of the $[EMIM]^+$ rings. However, the troughs at the center have values around −0.15 and −0.3 for the corresponding rigid (see Figure 5c) and flexible (see Figure 5f) confinements, respectively, which indicate that the rings are not perfectly parallel in the middle of the confinement. Also, we observe two broad peaks in the orientational order parameter of the $\overrightarrow{N_1N_2}$ vector, corresponding to perpendicular orientations of $[EMIM]^+$ rings. The alternating, layered structure of the troughs and peaks suggests an alternating pattern of parallel and perpendicular cation orientations between the confining solvophobic sheets. These observations are in good agreement with the interpretation of the number density profiles in Figure 4.

3.3. Structural Changes upon Capillary Evaporation.

The above examination of the average density and orientation in the liquid basin suggests that sheet flexibility has only a minor impact on the structure of the confined IL. This may be expected based on the free energy profiles in Figure 3. Significant differences between the rigid and flexible sheet systems appear when the number of ions in the confinement is decreased. Therefore, we additionally investigate the liquid structure between the solvophobic sheets as N is reduced. We focus on the joint density distribution, $\rho(z,\theta)$, where θ is the angle formed by the ring vector $\overrightarrow{N_1N_2}$ and the unit vector perpendicular to the confining surface. Representative results obtained for d = 1.3 nm are shown in Figure 6 for representative biasing values of N^*.

All joint density distributions show two major orientations of the cation rings between rigid and flexible sheets (parallel and perpendicular to the sheets), in agreement with the above analysis of the structure in the liquid basin. The cation rings adopt parallel orientations ($\theta \approx 90°$) near the sheet surface. In contrast, perpendicularly aligned rings ($\theta \approx 0, 180°$) are found near the center of the confined region.

Structural differences between the rigid and flexible sheet systems increase as N is decreased. Adding flexibility to the sheets results in an increase in the density of cation rings with perpendicular orientations in the center of the slab at low IL densities, as evidenced by Figure 6a,b for N^* = 10. The increase in cations with this orientation results indirectly from the decrease in the effective separation because of inward bending of the flexible sheets (see Section 3.1). At low N, a large vapor bubble exists in between and bridges the two sheets, and this vapor bubble creates a nanoscale liquid–vapor interface perpendicular to the plane of the confining sheets.[26,28,53,58,61] When the sheets are flexible, the smaller effective d results in a larger vapor bubble than the rigid plates for the same N^* and d and therefore more liquid–vapor interfacial surface area. At a liquid–vapor interface, $[EMIM]^+$ rings lie parallel to the surface.[62] In confinement, this orientation is adopted by cations at the nanoscale liquid–vapor interface of the vapor bubble, parallel to the vapor bubble interface and perpendicular to the sheets. This orientation is additionally favored by weak, attractive dispersion interactions between the $[EMIM]^+$ alkyl groups and the sheets.

4. CONCLUSIONS

The stability of an IL in nanoscale solvophobic confinement depends on the separation between the confining sheets. At larger separations, the liquid phase is stable and the vapor phase is metastable or unstable for very large separations. The critical distance below which the liquid phase of $[EMIM][BF_4]$ becomes metastable and the vapor phase becomes stable also depends on the flexibility of the confining material.[28,58] We have shown that flexible confining surfaces have relatively smaller free energy barriers for capillary evaporation of an IL confined between model solvophobic sheets. Our results also show that the effect of flexibility on the barrier height decreases at lower separation, consistent with the previous work on confined water.[28]

The confined IL is significantly structured, with layering of ions between the confining surfaces observed for all three intersheet spacings studied here. We find two major orientations of confined cations, with parallel alignment close to the surface and perpendicular alignment at the center of the confinement for d = 1.1 nm and d = 1.3 nm spacings. For d = 1.5 nm, five layers with alternating arrangements of parallel and perpendicular orientation of cation rings are observed. Through examination of the joint position and orientation density of cations as the confined IL density is decreased, we detail an interplay between the IL–sheet and IL–vapor bubble interfacial structure. At low N, cation rings lie perpendicular to the sheet surface and parallel to the IL–vapor interface created by a vapor bubble, and these orientations are more prevalent for flexible sheets than rigid sheets for the same d and biasing potential (N^*).

To conclude, we show that the mechanical properties of confining surfaces play a key role in controlling the thermodynamics of capillary evaporation of ILs in solvophobic confinement. Aside from the increased structuring in ILs that can significantly impact the d-dependence of free energy barriers,[26] the qualitative effects of surface flexibility are similar to those found for water.[28,58] Our results suggest that tuning the flexibility of solute particles can be employed to control

https://dx.doi.org/10.1021/acs.jpcc.9b11755
J. Phys. Chem. C 2020, 124, 4899–4906

self-assembly and introducing flexibility to the electrodes in EDLCs may alter their performance.

AUTHOR INFORMATION

Corresponding Author

Hemant K. Kashyap − *Department of Chemistry, Indian Institute of Technology Delhi, New Delhi 110016, India;* orcid.org/0000-0001-9124-2918; Phone: +91-(0)11-26591518; Email: hkashyap@chemistry.iitd.ac.in; Fax: +91-(0)11-26581102

Authors

Harender S. Dhattarwal − *Department of Chemistry, Indian Institute of Technology Delhi, New Delhi 110016, India;* orcid.org/0000-0001-6074-6734

Richard C. Remsing − *Department of Chemistry and Chemical Biology, Rutgers University, Piscataway, New Jersey 08854, United States;* orcid.org/0000-0002-0922-4882

Complete contact information is available at: https://pubs.acs.org/10.1021/acs.jpcc.9b11755

Notes

The authors declare no competing financial interest.

ACKNOWLEDGMENTS

H.S.D. thanks UGC India for fellowship. The authors thank the IIT Delhi HPC facility for computational resources. This work was financially supported by Science and Engineering Research Board (SERB), Department of Science and Technology, India, through the Core Research Grant (CRG/2019/000898) awarded to H.K.K.

REFERENCES

(1) Zein El Abedin, S.; Endres, F. Ionic Liquids: The Link to High-Temperature Molten Salts? *Acc. Chem. Res.* **2007**, *40*, 1106−1113.

(2) Davis, J. H., Jr. Task-Specific Ionic Liquids. *Chem. Lett.* **2004**, *33*, 1072−1077.

(3) Lei, Z.; Chen, B.; Koo, Y.-M.; MacFarlane, D. R. Introduction: Ionic Liquids. *Chem. Rev.* **2017**, *117*, 6633−6635.

(4) Simon, P.; Gogotsi, Y. Materials for Electrochemical Capacitors. *Nat. Mater.* **2008**, *7*, 845.

(5) Armand, M.; Endres, F.; MacFarlane, D. R.; Ohno, H.; Scrosati, B. Ionic-Liquid Materials for the Electrochemical Challenges of the Future. *Nat. Mater.* **2009**, *8*, 621.

(6) Lu, W.; Fadeev, A. G.; Qi, B.; Smela, E.; Mattes, B. R.; Ding, J.; Spinks, G. M.; Mazurkiewicz, J.; Zhou, D.; Wallace, G. G.; et al. Use of Ionic Liquids for pi-Conjugated Polymer Electrochemical Devices. *Science* **2002**, *297*, 983.

(7) MacFarlane, D. R.; Forsyth, M.; Howlett, P. C.; Pringle, J. M.; Sun, J.; Annat, G.; Neil, W.; Izgorodina, E. I. Ionic Liquids in Electrochemical Devices and Processes: Managing Interfacial Electrochemistry. *Acc. Chem. Res.* **2007**, *40*, 1165−1173.

(8) Weingärtner, H. Understanding Ionic Liquids at the Molecular Level: Facts, Problems, and Controversies. *Angew. Chem., Int. Ed.* **2008**, *47*, 654−670.

(9) Smiglak, M.; Metlen, A.; Rogers, R. D. The Second Evolution of Ionic Liquids: From Solvents and Separations to Advanced Materials−Energetic Examples from the Ionic Liquid Cookbook. *Acc. Chem. Res.* **2007**, *40*, 1182−1192.

(10) Greaves, T. L.; Kennedy, D. F.; Mudie, S. T.; Drummond, C. J. Diversity Observed in the Nanostructure of Protic Ionic Liquids. *J. Phys. Chem. B* **2010**, *114*, 10022−10031.

(11) Greaves, T. L.; Drummond, C. J. Solvent Nanostructure, the Solvophobic Effect and Amphiphile Self-Assembly in Ionic Liquids. *Chem. Soc. Rev.* **2013**, *42*, 1096−1120.

(12) He, Z.; Alexandridis, P. Nanoparticles in Ionic Liquids: Interactions and Organization. *Phys. Chem. Chem. Phys.* **2015**, *17*, 18238−18261.

(13) Zhao, Y.; Hu, Z. Graphene in Ionic Liquids: Collective van der Waals Interaction and Hindrance of Self-Assembly Pathway. *J. Phys. Chem. B* **2013**, *117*, 10540−10547.

(14) Xie, R.; Lpez-Barrn, C. R.; Wagner, N. J. *Ionic Liquids: Current State and Future Directions*; ACS Symposium Series; American Chemical Society, 2017; Vol. *1250*, pp 83−142.

(15) Bordes, E.; Morcos, B.; Bourgogne, D.; Andanson, J.-M.; Bussière, P.-O.; Santini, C. C.; Benayad, A.; Costa Gomes, M.; Pádua, A. A. H. Dispersion and Stabilization of Exfoliated Graphene in Ionic Liquids. *Front. Chem.* **2019**, *7*, 223.

(16) Kanduč, M.; Schlaich, A.; Schneck, E.; Netz, R. R. Water-Mediated Interactions between Hydrophilic and Hydrophobic Surfaces. *Langmuir* **2016**, *32*, 8767−8782.

(17) Liu, K.; Zhang, P.; Wu, J. Does Capillary Evaporation Limit the Accessibility of Nonaqueous Electrolytes to the Ultrasmall Pores of Carbon Electrodes? *J. Chem. Phys.* **2018**, *149*, 234708.

(18) Klinger, D.; Robb, M. J.; Spruell, J. M.; Lynd, N. A.; Hawker, C. J.; Connal, L. A. Supramolecular Guests in Solvent Driven Block Copolymer Assembly: from Internally Structured Nanoparticles to Micelles. *Polym. Chem.* **2013**, *4*, 5038−5042.

(19) Lum, K.; Chandler, D.; Weeks, J. D. Hydrophobicity at Small and Large Length Scales. *J. Phys. Chem. B* **1999**, *103*, 4570−4577.

(20) Li, Y.; Alibakhshi, M. A.; Zhao, Y.; Duan, C. Exploring Ultimate Water Capillary Evaporation in Nanoscale Conduits. *Nano Lett.* **2017**, *17*, 4813−4819.

(21) Li, Y.; Chen, H.; Xiao, S.; Alibakhshi, M. A.; Lo, C.-W.; Lu, M.-C.; Duan, C. Ultrafast Diameter-Dependent Water Evaporation from Nanopores. *ACS Nano* **2019**, *13*, 3363−3372.

(22) Kieu, H. T.; Liu, B.; Zhang, H.; Zhou, K.; Law, A. W.-K. Molecular Dynamics Study of Water Evaporation Enhancement Through a Capillary Graphene Bilayer with Tunable Hydrophilicity. *Appl. Surf. Sci.* **2018**, *452*, 372−380.

(23) Wallqvist, A.; Berne, B. J. Computer Simulation of Hydrophobic Hydration Forces on Stacked Plates at Short Range. *J. Phys. Chem.* **1995**, *99*, 2893−2899.

(24) Cerdeiriña, C. A.; Debenedetti, P. G.; Rossky, P. J.; Giovambattista, N. Evaporation Length Scales of Confined Water and Some Common Organic Liquids. *J. Phys. Chem. Lett.* **2011**, *2*, 1000−1003.

(25) Chandler, D. Interfaces and the Driving Force of Hydrophobic Assembly. *Nature* **2005**, *437*, 640−647.

(26) Shrivastav, G.; Remsing, R. C.; Kashyap, H. K. Capillary Evaporation of the Ionic Liquid [EMIM] [BF_4] in Nanoscale Solvophobic Confinement. *J. Chem. Phys.* **2018**, *148*, 193810.

(27) Huang, X.; Margulis, C. J.; Berne, B. J. Dewetting-Induced Collapse of Hydrophobic Particles. *Proc. Natl. Acad. Sci. U.S.A.* **2003**, *100*, 11953.

(28) Altabet, Y. E.; Haji-Akbari, A.; Debenedetti, P. G. Effect of Material Flexibility on the Thermodynamics and Kinetics of Hydrophobically Induced Evaporation of Water. *Proc. Natl. Acad. Sci. U.S.A.* **2017**, *114*, E2548−E2555.

(29) Palacio, M.; Bhushan, B. A Review of Ionic Liquids for Green Molecular Lubrication in Nanotechnology. *Tribol. Lett.* **2010**, *40*, 247−268.

(30) Somers, A.; Howlett, P.; MacFarlane, D.; Forsyth, M. A Review of Ionic Liquid Lubricants. *Lubricants* **2013**, *1*, 3−21.

(31) Sharma, S.; Kashyap, H. K. Structure of Quaternary Ammonium Ionic Liquids at Interfaces: Effects of Cation Tail Modification with Isoelectronic Groups. *J. Phys. Chem. C* **2015**, *119*, 23955−23967.

(32) Sharma, S.; Kashyap, H. K. Interfacial Structure of Pyrrolidinium Cation Based Ionic Liquids at Charged Carbon Electrodes: The Role of Linear and Nonlinear Alkyl Tails. *J. Phys. Chem. C* **2017**, *121*, 13202−13210.

(33) Sharma, S.; Dhattarwal, H. S.; Kashyap, H. K. Molecular Dynamics Investigation of Electrostatic Properties of Pyrrolidinium

Cation Based Ionic Liquids Near Electrified Carbon Electrodes. *J. Mol. Liq.* **2019**, *291*, 111269.
(34) Mousavi, M. P. S.; Wilson, B. E.; Kashefolgheta, S.; Anderson, E. L.; He, S.; Bühlmann, P.; Stein, A. Ionic Liquids as Electrolytes for Electrochemical Double-Layer Capacitors: Structures that Optimize Specific Energy. *ACS Appl. Mater. Interfaces* **2016**, *8*, 3396−3406.
(35) Orita, A.; Kamijima, K.; Yoshida, M. Allyl-Functionalized Ionic Liquids as Electrolytes for Electric Double-Layer Capacitors. *J. Power Sources* **2010**, *195*, 7471−7479.
(36) Lockett, V.; Sedev, R.; Ralston, J.; Horne, M.; Rodopoulos, T. Differential Capacitance of the Electrical Double Layer in Imidazolium-Based Ionic Liquids: Influence of Potential, Cation Size, and Temperature. *J. Phys. Chem. C* **2008**, *112*, 7486−7495.
(37) Balducci, A.; Bardi, U.; Caporali, S.; Mastragostino, M.; Soavi, F. Ionic Liquids for Hybrid Supercapacitors. *Electrochem. Commun.* **2004**, *6*, 566−570.
(38) Lewandowski, A.; Galiński, M. Carbon-Ionic Liquid Double-Layer Capacitors. *J. Phys. Chem. Solids* **2004**, *65*, 281−286.
(39) Lazzari, M.; Soavi, F.; Mastragostino, M. High Voltage, Asymmetric EDLCs Based on Xerogel Carbon and Hydrophobic IL Electrolytes. *J. Power Sources* **2008**, *178*, 490−496.
(40) Noh, C.; Jung, Y. Understanding the Charging Dynamics of an Ionic Liquid Electric Double Layer Capacitor via Molecular Dynamics Simulations. *Phys. Chem. Chem. Phys.* **2019**, *21*, 6790−6800.
(41) Katsyuba, S. A.; Dyson, P. J.; Vandyukova, E. E.; Chernova, A. V.; Vidi, A. Molecular Structure, Vibrational Spectra, and Hydrogen Bonding of the Ionic Liquid 1-Ethyl-3-methyl-1H-imidazolium Tetrafluoroborate. *Helv. Chim. Acta* **2004**, *87*, 2556−2565.
(42) Han, D.; Row, K. H. Recent Applications of Ionic Liquids in Separation Technology. *Molecules* **2010**, *15*, 2405−2426.
(43) Valencia, H.; Kohyama, M.; Tanaka, S.; Matsumoto, H. Ab Initio Study of [EMIM] [BF_4] Molecule Adsorption on Li Surfaces as a Model for Ionic Liquid/Li Interfaces in Li-ion Batteries. *Phys. Rev. B: Condens. Matter Mater. Phys.* **2008**, *78*, 205402.
(44) Heimer, N. E.; Del Sesto, R. E.; Meng, Z.; Wilkes, J. S.; Carper, W. R. Vibrational Spectra of Imidazolium Tetrafluoroborate Ionic Liquids. *J. Mol. Liq.* **2006**, *124*, 84−95.
(45) Martínez, L.; Andrade, R.; Birgin, E. G.; Martínez, J. M. PACKMOL: A Package for Building Initial Configurations for Molecular Dynamics Simulations. *J. Comput. Chem.* **2009**, *30*, 2157−2164.
(46) Berendsen, H. J. C.; van der Spoel, D.; van Drunen, R. GROMACS: A message-passing parallel molecular dynamics implementation. *Comput. Phys. Commun.* **1995**, *91*, 43−56.
(47) van der Spoel, D.; Lindahl, E.; Hess, B.; Groenhof, G.; Mark, A. E.; Berendsen, H. J. C. GROMACS: Fast, Flexible, and Free. *J. Comput. Chem.* **2005**, *26*, 1701−1718.
(48) Berendsen, H. J. C.; Postma, J. P. M.; van Gunsteren, W. F.; DiNola, A.; Haak, J. R. Molecular Dynamics with Coupling to an External Bath. *J. Chem. Phys.* **1984**, *81*, 3684−3690.
(49) Parrinello, M.; Rahman, A. Polymorphic Transitions in Single Crystals: A New Molecular Dynamics Method. *J. Appl. Phys.* **1981**, *52*, 7182−7190.
(50) Nosé, S. A Unified Formulation of the Constant Temperature Molecular Dynamics Methods. *J. Chem. Phys.* **1984**, *81*, 511−519.
(51) Hoover, W. G. Canonical Dynamics: Equilibrium Phase-Space Distributions. *Phys. Rev. A* **1985**, *31*, 1695−1697.
(52) Humphrey, W.; Dalke, A.; Schulten, K. VMD − Visual Molecular Dynamics. *J. Mol. Graphics* **1996**, *14*, 33−38.
(53) Remsing, R. C.; Xi, E.; Vembanur, S.; Sharma, S.; Debenedetti, P. G.; Garde, S.; Patel, A. J. Pathways to Dewetting in Hydrophobic Confinement. *Proc. Natl. Acad. Sci. U.S.A.* **2015**, *112*, 8181−8186.
(54) Canongia Lopes, J. N.; Deschamps, J.; Pádua, A. A. H. Modeling Ionic Liquids Using a Systematic All-Atom Force Field. *J. Phys. Chem. B* **2004**, *108*, 2038−2047.
(55) Patel, A. J.; Varilly, P.; Chandler, D.; Garde, S. Quantifying Density Fluctuations in Volumes of all Shapes and Sizes Using Indirect Umbrella Sampling. *J. Stat. Phys.* **2011**, *145*, 265−275.
(56) Patel, A. J.; Varilly, P.; Chandler, D. Fluctuations of Water near Extended Hydrophobic and Hydrophilic Surfaces. *J. Phys. Chem. B* **2010**, *114*, 1632−1637.
(57) Kumar, S.; Rosenberg, J. M.; Bouzida, D.; Swendsen, R. H.; Kollman, P. A. The Weighted Histogram Analysis Method for Free-Energy Calculations on Biomolecules. I. the Method. *J. Comput. Chem.* **1992**, *13*, 1011−1021.
(58) Altabet, Y. E.; Debenedetti, P. G. The Role of Material Flexibility on the Drying Transition of Water Between Hydrophobic Objects: A Thermodynamic Analysis. *J. Chem. Phys.* **2014**, *141*, 18C531.
(59) Alibalazadeh, M.; Foroutan, M. Specific Distributions of Anions and Cations of an Ionic Liquid Through Confinement Between Graphene Sheets. *J. Mol. Model.* **2015**, *21*, 168.
(60) Altabet, Y. E.; Debenedetti, P. G. Communication: Relationship between Local Structure and the Stability of Water in Hydrophobic Confinement. *J. Chem. Phys.* **2017**, *147*, 241102.
(61) Sharma, S.; Debenedetti, P. G. Free Energy Barriers to Evaporation of Water in Hydrophobic Confinement. *J. Phys. Chem. B* **2012**, *116*, 13282−13289.
(62) Yan, T.; Li, S.; Jiang, W.; Gao, X.; Xiang, B.; Voth, G. A. Structure of the Liquid Vacuum Interface of Room-Temperature Ionic Liquids: A Molecular Dynamics Study. *J. Phys. Chem. B* **2006**, *110*, 1800−1806.

https://dx.doi.org/10.1021/acs.jpcc.9b11755
J. Phys. Chem. C 2020, 124, 4899−4906